RSC Advances

PAPER

View Article Online
View Journal | View Issue

Cite this: *RSC Adv.*, 2022, **12**, 27855

Elucidating the roles of oxygen functional groups and defect density of electrochemically exfoliated GO on the kinetic parameters towards furazolidone detection†

Dao Thi Nguyet Nga, ‡[a] Nguyen Le Nhat Trang, ‡[a] Van-Tuan Hoang, *[a] Xuan-Dinh Ngo, [a] Pham Tuyet Nhung, [a] Doan Quang Tri,[c] Nguyen Duy Cuong,[c] Pham Anh Tuan,[d] Tran Quang Huy [a] and Anh-Tuan Le *[ab]

Received 5th July 2022
Accepted 21st September 2022

DOI: 10.1039/d2ra04147b

rsc.li/rsc-advances

Using electrochemically exfoliated graphene oxide (GO)-modified screen-printed carbon electrodes for the detection of furazolidone (FZD), a nitrofuran antibiotic, was explored. In this study, we designed some GO samples possessing different oxygen functional group content/defect density by using ultrasonic irradiation or microwave techniques as supporting tools. The difference in physical characteristics of GO led to the remarkable change in kinetic parameters (electron transfer rate constant (k_s) and transfer coefficient (α)) of electron transfer reactions at K_3/K_4 probes as well as the FZD analyte. Obtained results reveal that the GO-ultrasonic sample showed the highest electrochemical response toward FZD detection owing to the increase in defect density and number of edges in the GO nanosheets under ultrasonic irradiation. The proposed electrochemical nanosensor enabled the monitoring of FZD in the linear range from 1 μM to 100 μM with an electrochemical sensitivity of 1.03 μA μM^{-1} cm^{-2}. Tuning suitable electronic structures of GO suggests the potentiality of advanced GO-based electrochemical nanosensor development in food-producing animal safety monitoring applications.

1. Introduction

Electrochemical sensor techniques have been reported as an effective tool for the detection of biomolecules, heavy metal ions, and environmental pollutants due to their affordable cost, the small amount of analyte required, and their excellent detection limits, robustness, fast detection process, ease of use, and environmental friendliness.[1] However, this method still has disadvantages such as poor sensitivity and selectivity faced at the bare electrodes. To overcome this weakness, many nanomaterials with unique properties have been used to modify the bare electrode surface to enhance the electrochemical behavior of sensors[2,3]. Li *et al.*[4] have modified a glassy carbon electrode (GCE) using single-walled carbon nanotubes (SWCNTs) for the detection of dopamine. The obtained results show that the oxidation peak currents of SWCNTs/GCE significantly increased compared to these peaks of the bare electrode. In another report, Dos Santos *et al.*[5] have reported GCE modification using 3D graphene to improve the detection of dopamine. Besides the factors such as the abundant number of structural defects and edge planes, the interaction between the residual oxygen functional group on the 3D graphene surface and dopamine is an important factor to improve dopamine detection performance. Similarly, Arumugasamy *et al.*[6] have also used nanocomposites of graphene quantum dots (GQDs) and multiwall carbon nanotubes (MWCNTs) for electrochemical sensing of dopamine. In this study, GQDs@MWCNTs/GCE not only enhanced the electrochemical signal but also increased the electrocatalytic activity toward dopamine detection. The above results suggest that for a given analysis, the selection of suitable nanomaterials for electrode modification has a great role in the detection performance of electrochemical sensors.

Over the last decade, two-dimensional nanomaterials such as molybdenum disulfide (MoS_2), two-dimensional transition metal dichalcogenides (TMDs), and graphene oxide (GO) with their unique physicochemical properties have been used as nanoplatforms in electrochemical sensors[3,7–9]. Among them, GO is one of the common 2D nanomaterials to select for

[a]*Phenikaa University Nano Institute (PHENA), PHENIKAA University, Hanoi 12116, Vietnam. E-mail: tuan.hoangvan@phenikaa-uni.edu.vn; tuan.leanh@phenikaa-uni.edu.vn*

[b]*Faculty of Materials Science and Engineering (MSE), PHENIKAA University, Hanoi 12116, Vietnam*

[c]*International Training Institute for Materials Science (ITIMS), Hanoi University of Science and Technology (HUST), 1st Dai Co Viet Road, Hanoi, Viet Nam*

[d]*Faculty of Biotechnology, Chemical and Environmental Engineering (BCCE), PHENIKAA University, Vietnam & Vicostone Joint Stock Company, Phenikaa Group, Hanoi 12116, Vietnam*

† Electronic supplementary information (ESI) available. See https://doi.org/10.1039/d2ra04147b

‡ D. T. N. Nga and N. L. N. Trang contributed equally to this work.

modification of the electrode surface due to its large surface area, good conductivity, chemical stability, and strong mechanical strength.[10–13] The GO modified-electrode not only enhances the redox peak current but also increases absorption capacity for the sensitive detection of many analyte molecules such as 4-nitrophenol,[14] naptalam,[15] or naproxen.[16] In fact, some recent articles have shown that the performance of GO-based electrochemical sensors has strongly depended on the changes in the microstructure of GO.[17,18] Thus, controlling synthesis conditions is significantly important for their applicability in electrochemical sensors. Normally, the synthesis of GO and rGO was performed through wet chemical methods with the utilization of some hazardous chemicals such as H_2SO_4, $KMnO_4$, and hydrazine, which is a potential risk for human health and the environment and is also time-consuming for fabrication.[19] From this fact, we proposed the GO preparation by an electrochemical exfoliation method, which possesses many advantages of simplicity and environmental friendliness. Instead of focusing on enhancing the electrochemical performance of GO-modified electrodes as in previous reports, in this case, simple ultrasonic irradiation or microwave techniques were used as supporting tools aiming to create the changes in the microstructure of GO, for example, the concentration of functional groups containing oxygen on the GO surface, the number of edges, disorder degree, and defect density of the carbon framework. More importantly, by comparing and analyzing these parameters in electrochemical conditions, their remarkable impacts on the electrokinetic parameters (the electron transfer rate constant (k_s) and the transfer coefficient (α)) for electron transfer reaction of K_3/K_4 probes and the furazolidone analyte were observed. This study is expected to show the nature and role of changes in the microstructure of GO for electrochemical sensing applications.[20–22] In addition, ultrasound, and microwave irradiation techniques had also been used as supporting tools to design some GO samples with different structural properties. These techniques allow controlling systemic changes well in the electronic structure of graphene materials.[23–26]

Furazolidone (FZD) is a nitrofuran antibiotic that has been used as a drug for the treatment of bacterial infections in livestock production.[27,28] Due to its damage to human health, FZD has been prohibited in livestock by the European Commission since 1995.[29] However, due to low cost and high effectiveness, FZD is still illegally employed in livestock farms.[30] Thus, the development of rapid analysis techniques with low cost, high reliable results is still interestingly challenging to help in monitoring FZD residues in food-producing animals.

Herein, for the first time, we systematically studied the roles of the oxygen functional groups and defect density on the analytical kinetic parameters of the FZD electrochemical reduction process. A detailed understanding of the impact of the above factors helps to orient the more suitable design of GO-based electrode materials for applications in electrochemical sensing devices. Finally, the relationship between the kinetic parameters and the detection capacity of FZD was discussed in detail.

2. Experimental procedures

2.1. Chemicals

A carbon graphite sheet ($L \times W \times T = 50$ mm $\times$ 50 mm $\times$ 5 mm) was obtained from Tooling House Store, Chinese and a bulk silver bar ($L \times W \times T = 150$ mm $\times$ 10 mm $\times$ 0.5 mm) was used as electrodes, which was purchased from a domestic jewellery company in Hanoi, Vietnam. Ammonium sulfate ($(NH_4)_2SO_4$ > 98%) was purchased from Shanghai Chemical Reagent. Furazolidone (FZD > 98%) was provided by Sigma-Aldrich. The PBS buffer solutions (0.1 M, pH 7.2) were prepared using NaCl, KCl, $Na_2HPO_412H_2O$, and KH_2PO_4 (>99%, Merck KGaA, Germany). The pH value of the PBS buffer was adjusted by H_3PO_4 (0.1 M) and NaOH (2 M). Carbon screen-printed electrodes (SPEs-DS110) were purchased from DS Dropsens, Spain.

2.2. Electrochemical exfoliation of GO nanosheets

The silver (or graphite) cathode is immersed in 700 mL of 0.1 M ammonium sulfate $(NH_4)_2SO_4$ aqueous solution as an electrolyte. A carbon graphite sheet is an anode. Two electrodes were installed parallel to each other and immersed in the electrolyte. Both anode and cathode electrodes were connected to a power supply (7 V). Electrochemical expansion time was 8 hours. The product of the electrochemical process is graphene oxide aqueous solution (GO-1). The GO-2 sample was obtained from the GO-1 sample after ultrasound treatment with 50 kHz for 15 minutes. The GO-3 sample was obtained by treating the GO-1 sample using UWave-2000 multifunctional microwave for 15 minutes with 250 W at 80 °C.

2.3. Preparation of real samples

Pork samples were purchased from the local supermarket and homogenized thoroughly before extraction. Next, 5 g of homogenized pork sample was mixed with 10 mL phosphate buffer solution (0.1 M) by a vortex mixer, and this solution was ultrasonicated for 30 min. The solution was centrifuged for 5 min at 10 000 rpm and the clear liquid phase was collected. Finally, the known different amounts (10, 25, 50 μM) of FZD standard were added.

2.4. Characterization techniques

The graphene oxide (GO) formation was confirmed by an ultraviolet-visible (UV-vis) spectrophotometry (HP 8453 spectrophotometer). The morphology of GO was observed *via* scanning electron microscopy (JEOL JSM-7600F). The Raman measurements were performed by Raman spectroscopy (MacroRam, Horiba Scientific). Fourier transform infrared spectroscopy (FTIR) spectra were recorded using an IRAffinity-1S spectrometer. Measurements of the pH values were performed with an IC-PH60 pH tester kit.

2.5. Electrochemical measurements

All electrochemical measurements were performed using an electrochemical workstation (Palmsens4, PS Trace, PalmSens,

The Netherlands) at room temperature. Cyclic voltammetry (CV) measurements were carried out in 0.1 M KCl containing 5 mM $[Fe(CN)_6]^{3-/4-}$ at a scan rate of 50 mV.s^{-1} with a potential range from −0.3 V to −0.6 V. Electrochemical impedance spectroscopy (EIS) was recorded in the frequency range of 0.01–50 kHz by applying an AC voltage with 10 mV amplitude in 0.1 M KCl containing 5 mM $[Fe(CN)_6]^{3-/4-}$. The electrochemical performance of FZD on the modified and unmodified electrodes with GO, GO-2, and GO-3 was investigated using CV and linear sweep voltammetry (LSV) measurements in an aqueous phosphate buffer electrolyte solution (PBS, 0.1 M, pH-5). The CV was obtained at a scan rate of 50 mV s^{-1} in the potential range from −1.1 to 0 V, $T_{equilibrium}$ = 50 s. Similarly, the LSV measurement was completed at conditions as follows: scan rate of 50 mV.s^{-1}, $T_{equilibrium}$ = 120 s, in the potential range of −0.2 to −0.9 V.

An initial solution of FZD with a concentration of 1000 μM was prepared by dissolving 5.629 mg of FZD in 25 mL of 30% dimethyl formamide solution, under the aid of magnetic stirring for 30 min at room temperature.

3. Results and discussion

3.1. Microstructure and characterization

To study the impact of oxygen functional group and defect density of graphene oxide (GO) on the electrochemical behaviors of furazolidone, three GO samples with the difference in the oxygen functional groups and defect density were prepared by an electrochemical exfoliating method, and then were treated with ultrasonic or microwave techniques. Fig. 1 shows the UV-vis absorption spectra of the prepared GO samples. The GO-1 sample which was directly obtained by an electrochemical exfoliating method exhibited an absorption peak at 230 nm due to the π–π* transition of the aromatic C=C ring and a weak broad absorption shoulder around 300 nm attributed to the n–π* transition of C=O bonds in sp^3 hybrid regions.[31] The GO-2 and GO-3 also exhibited a similar absorption spectrum to the GO absorption spectrum, with a strong absorption peak at 230 nm and a weak absorption shoulder at 300 nm. Moreover, the decrease of the C=O characteristic absorption peak at 300 nm demonstrated a decrease in the oxygen content of treated GO samples.[32] However, the C=C characteristic absorption peak of treated GO samples was slightly shifted to a shorter wavelength, indicating that the conjugated electron structure of GO is not fully restored.[32]

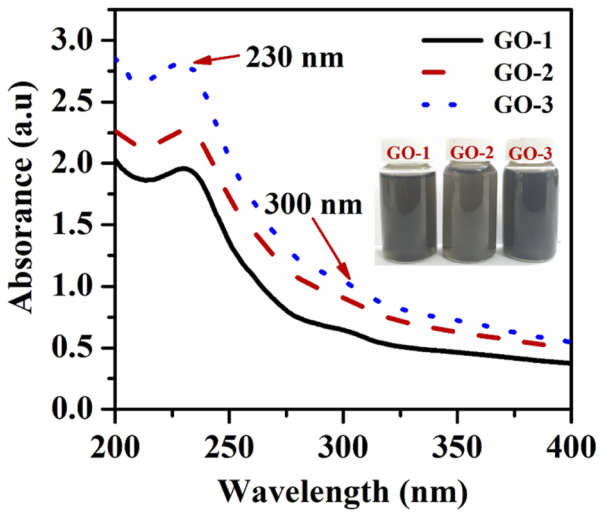

Fig. 1 UV-vis spectra of GO-1, GO-2, and GO-3 samples.

Raman spectroscopy analysis helps to determine the microstructural properties of GO, such as oxygen content, crystallinity, and disorder degree. The Raman spectra of GO-1, GO-2, and GO-3 were shown in Fig. 2(a–c). All the spectra presented two noticeable peaks at ∼1313 and ∼1605 cm^{-1}, which corresponded to the D and G bands, respectively. The G peak corresponded to the high-frequency E_{2g} phonon at the Brillouin zone centre, while the D peak corresponded to the defects or disordered carbons of six-atom rings due to sp^3 – bonded carbon atoms or impurities.[33–35] The ratio between the intensity of the D band and the G band was calculated to determine the disorder level or defects in the GO structure.[36] The I_D/I_G ratio of GO-1, GO-2, and GO-3 were 1.6, 1.67, and 1.4, respectively. The obtained results show that the GO-2 sample has a higher disorder degree and defect density than that of GO-1, which can be attributed due to the impact of ultrasound irradiation causes the fragmentation of the carbon framework. The lower defect level for the GO-3 sample suggests that microwave irradiation can restore the sp^2 hybridized carbons of graphene from the reduced oxygen functional groups on the GO surface. However, recent reports demonstrate that the presence of a new shoulder between D and G peaks is important in the interpretation of the Raman spectrum of GO[37],[38]. This shoulder is often neglected in the Raman spectral analysis of graphene derivatives because it is very weak. Herein, we fitted this shoulder using four

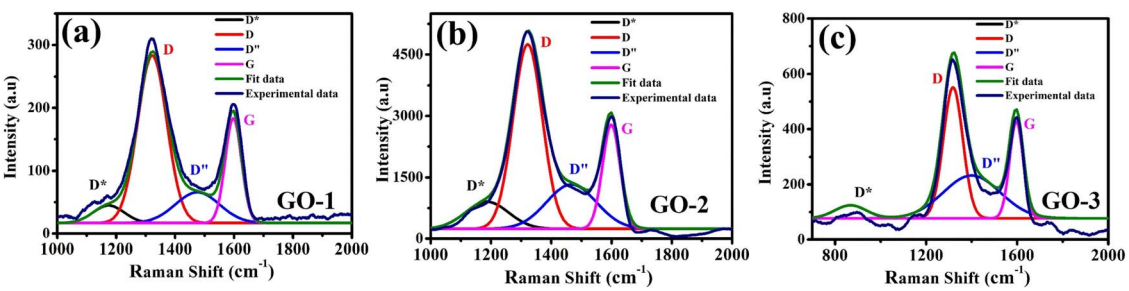

Fig. 2 Raman spectra of GO-1 (a), GO-2 (b), and GO-3 (c) samples.

functions which were ascribed to D^* ($\sim$1000 − 1200 cm^{-1}), D, D'' ($\sim$1450 − 1550 cm^{-1}), and G bands. Our obtained results show good agreement between the experimental spectrum and that calculated as a sum of the four proposed functions (Fig. 2(a–c)). These bands parameters such as position, intensity ratio, and width have related the microstructural properties such as oxygen content, crystallinity, and disorder degree of GO samples. According to Claramunt *et al.*,[37] the D'' band was related to amorphous phases since its intensity and width decreased in the increase of the crystallinity of the sheet. The $I_{D'}/I_G$ ratio values of GO-2 (0.42) and GO-3 (0.44) samples were significantly greater than that of GO-1 (0.29), suggesting the higher disorder degree of GO-2 and GO-3 samples. Results show a similar trend to that observed for the FWHM values. It was demonstrated that the D^* band was related to the disordered graphitic lattice of soot provided by the existence of sp^3 bonds.[37,38] The I_{D^*}/I_G ratio of the GO-3 (0.13) sample was significantly lower than that of GO-2 (0.26), suggesting the lower oxygen functional group content of the GO-3 sample. The obtained results show that microwave irradiation played a critical role in removing the oxygen functional group, while ultrasonic irradiation caused the damaged carbon framework. The changes in the structural property of GO have crucial effects on their electrochemical characteristics, which were investigated in more detail in the subsequent contents. This further result was confirmed *via* EDS data. Indeed, EDS measurement was performed to define the elemental composition of the proposed materials (Fig. S1†). The characteristic peak positions of elements C and O of GO-1, GO-2 and GO-3 samples were observed through the EDS spectrum. The percentages of C and O atoms were calculated as listed in Table S1.† Herein, there was a remarkable difference in the percentage of C and O atoms in GO-1, GO-2, and GO-3 samples. In which, the GO-3 sample contained the lowest ratio of O atoms meanwhile the highest ratio was achieved in the GO-1 sample. This result was accordant with other analytical results for the elemental composition of the various GO samples. The 2D structure of GO samples was observed *via* TEM and SEM images (Fig. S2†). As shown in Fig. S2a,† the typical morphology of the GO-1 sample was characterized by wrinkled and folded features. The uniform covering of the GO-1 sample on the SPE surface was clearly illustrated in Fig. S2b.† These GO nanosheets existed in overlapping or coalescing together as exfoliated and wrinkled layers.

The presence of the oxygen functional groups on the GO-1, GO-2, and GO-3 surfaces were observed using FTIR analysis. As shown in Fig. 3, the spectra of GO-1 and GO-2 samples showed some typical oxygen functional group peaks at 1039 cm^{-1} (C–O–C epoxy groups),[39] 1080 cm^{-1} (C–OH groups),[40] and 2359 cm^{-1} (CO_2 groups).[41] The absorption peak at 1635 cm^{-1} was assigned for the plane vibrations of sp^2-hybridized C=C.[39] The relatively broadband at 3240–3390 cm^{-1} was attributed to the adsorbed water on the surface of GO.[40,42,43] However, a noticeable decrease in the intensity of the adsorption bands of the oxygen functional groups was found for that GO-2 sample, suggesting the lower content of oxygen functional groups in this sample. The GO-3 spectrum exhibited only three peaks at 2359 cm^{-1} (CO_2 groups), 1635 cm^{-1} (C=C), and 1080 cm^{-1} (C–OH), which

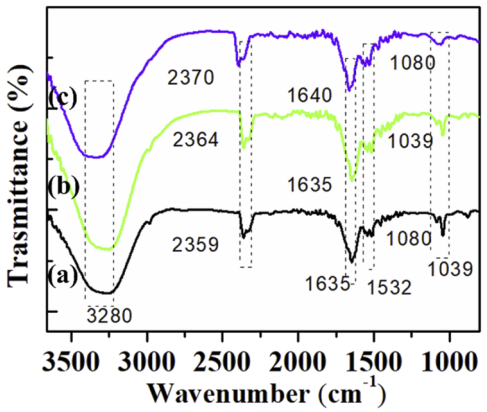

Fig. 3 FTIR spectrum of GO-1 (a), GO-2 (b), and GO-3 (c) samples.

suggests that some oxygen functional groups on the GO surface were removed. This result was in good agreement with the above Raman analysis. Our obtained results confirmed the destructed oxygen functional groups on the surface of GO when using ultrasound and microwave irradiation as supporting techniques. The oxygen functional group content could affect the electron transfer kinetics and the analyte adsorption of modified electrodes that will be analyzed in the electrochemical investigations.

3.2. Electrochemical investigations

3.2.1. Electrochemical characteristics of the modified electrodes. To understand from a fundamental point of view the structure parameters affecting the electrochemical behaviors of FZD, the electrochemical properties of the SPE electrodes modified with three different GO samples, including GO-1, GO-2, and GO-3 were investigated by CV and EIS techniques using a benchmark redox probe, $[Fe(CN)_6]^{3-/4-}$. Fig. 4a shows comparative cyclic voltammetric (CV) behaviors of bare SPE, GO-1/SPE, GO-2/SPE, and GO-3/SPE in 0.1 M KCl containing 5 mM $[Fe(CN)_6]^{3-/4-}$ at a scan rate of 50 mV.s^{-1}. It can be seen that all curves showed a pair of well-defined redox peaks corresponded to the electron transfer of Fe^{2+} reversibly into Fe^{3+} and *vice versa*. The calculated cathodic peak current intensities for bare SPE, GO-1/SPE, GO-2/SPE, and GO-3/SPE were about −127 μA, −170 μA, −160 μA, and −158 μA, respectively. Clearly, there was a remarkable enhancement in redox peak current response for all the modified SPEs. The GO-1/SPE showed the highest cathodic peak current intensity, which could be attributed to more oxygen functional group content, offering higher adsorption capacity. In addition, the peak-to-peak separation (ΔE_{pp}) values of GO-1/SPE, GO-2/SPE, and GO-3/SPE were found to be 194 mV, 173 mV, and 183 mV, respectively. The peak-to-peak potential separation and deviation from its theoretical value of zero can be utilized as critical proof of the limitations in the charge-transfer kinetics.[44,45] The large potential separation in GO-1/SPE could arise from the dominance of electrostatic factors, the side interactions of the redox couples, and even due to the presence of non-equivalent sites. The decrease in the ΔE_{pp} value of the GO samples treated with ultrasound and microwave suggested a faster electron transfer rate.[44,45]

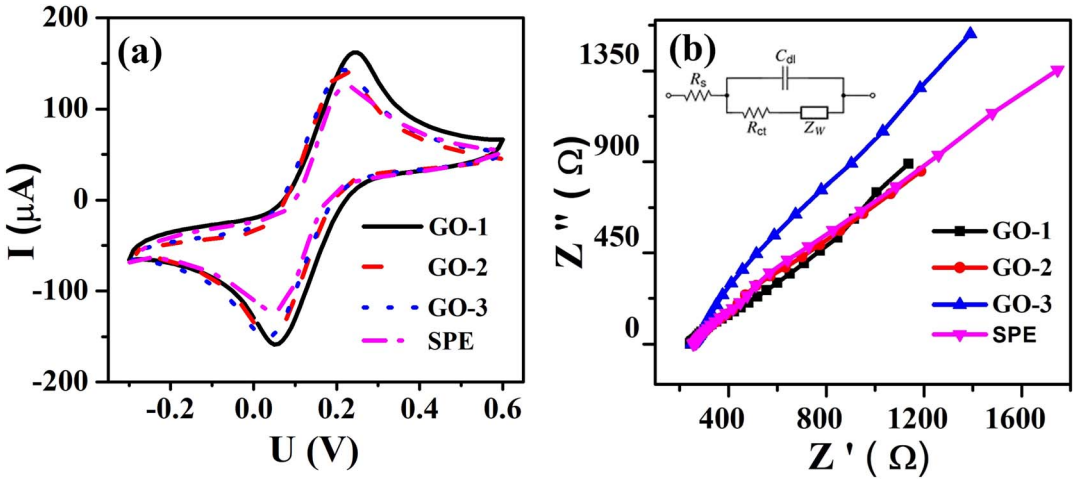

Fig. 4 (a) CV profiles of bare SPE and the modified SPEs at scan rate 50 mV s^{-1} in 0.1 M KCl containing 5 mM $[Fe(CN)_6]^{3-/4-}$; (b) EIS profiles of bare SPE and the modified SPEs.

The charge-transfer (R_{ct}) properties at the electrolyte-catalyst/electrode interface were evaluated using the electrochemical impedance spectroscopy (EIS) measurements.[46] Fig. 4b displays the Nyquist diagrams of bare SPE, GO-1/SPE, GO-2/SPE, and GO-3/SPE in the presence of 5 mM of $[Fe(CN)_6]^{3-/4-}$ containing 0.1 M of KCl with a constant AC potential of 10 mV and the frequency range from 0.1 Hz to 50 kHz. The equivalent circuit parameters were obtained by using Randles circuit as a fitting model in EIS analysis. This comparable circuit encompassed a double-layer capacitance (C_{dl}) related to the charging and background current, the ohmic resistance of the electrolyte (R_s), the charge-transfer resistance (R_{ct}) across the electrode–electrolyte interface, and the Warburg impedance (Z_w). The R_{ct} values of bare SPE, GO-1/SPE, GO-2/SPE, and GO-3/SPE were found to be 1963 Ω, 821.4 Ω, 1008 Ω, and 1888 Ω, respectively. The modification of SPEs with GO improved the electron transfer ability through electrode–electrolyte interface. Moreover, it was observed the significant difference in the electron transfer kinetic of modified SPEs. It is clear that the electronic structure of GO nanosheet was significantly changed under the impacts of ultrasonic and microwave irradiation. The higher R_{ct} value for the GO-3 sample could be attributed to the higher disorder degree of carbon framework and lower oxygen functional group content, resulting in a significant decline in both capacity and kinetic rate for analyte adsorption. To study the redox reaction process, CV curves were recorded on the modified SPEs in 0.1 M KCl containing 5 mM $[Fe(CN)_6]^{3-/4-}$ with various scan rates from 10 to 60 mV s^{-1}, as shown in Fig. 5. The observed peak currents (I_{pa} and I_{pc}) increased with increasing scan rate from 10 to 60 mV.s^{-1}. It was

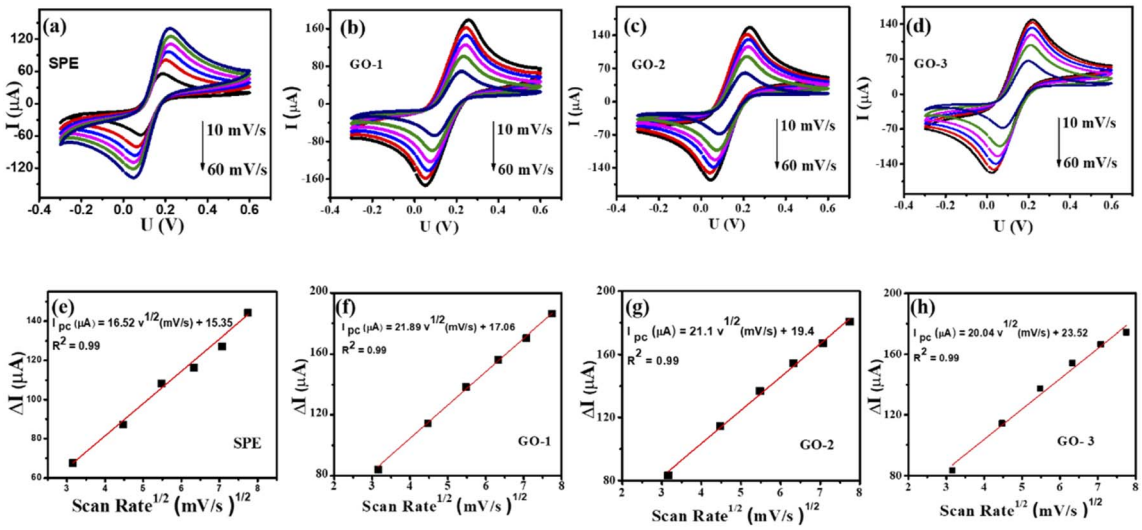

Fig. 5 (a–d) CV profiles of bare SPE and the modified SPEs at various scan rates (10–60 mVs^{-1}); and (e–h) the corresponding linear plot of reduction peak current response and sqrt of scan rate of bare SPE, GO-1/SPE, GO-2/SPE, and GO-3/SPE. All experiments were performed in 0.1 M KCl containing 5 mM $[Fe(CN)_6]^{3-/4-}$.

observed an excellent linear dependence of the peak current on the square root of the scan rate, suggesting the redox reaction at all the electrodes was the diffusion-controlled process (Fig. 5(e–h)). The electroactive surface area (EASA) is a very important factor affecting the electrochemical behaviors of FZD at the modified SPEs surface.[47] The EASA value of the modified SPEs was determined by using the Randles–Sevick equation (25 °C):

$$I_p = 2.69 \times 10^5\ A\ n^{3/2}\ D^{1/2}\ C\ v^{1/2} \quad (1)$$

where I_p presents the cathodic and anodic peak current, n is the number of electron transfer, D is diffusion coefficient of $[Fe(CN)_6]^{3-/4-}$, A is EASA, v is the potential scan rate, and C is the concentration of $[Fe(CN)_6]^{3-/4-}$. Herein, EASA values were estimated from the graphs of cathodic peak current along with $n = 1$, $D = 6.5 \times 10^{-6}$ cm.s^{-1}, and $C = 5$ mM. The estimated EASA values of bare SPE, GO-1/SPE, GO-2/SPE, and GO-3/SPE were 0.48 cm^2, 0.638 cm^2, 0.615 cm^2, and 0.58 cm^2, respectively. When GO was treated by microwave and ultrasonic irradiation, the electroactive surface area was decreased, which could be attributed to the removal of oxygen functional groups. This is consistent with the recorded EIS results at the modified SPEs.

3.2.2. Electrochemical behaviors of FZD on the modified electrodes. Fig. 6a shows CV curves of bare SPE, GO-1/SPE, GO-2/SPE, and GO-3/SPE in 100 μM FZD. There were no redox peaks recorded in the absence of FZD. The reduction peak current responses for bare SPE, GO-1/SPE, GO-2/SPE, and GO-3/SPE were about −3.65 μA, −6.41 μA, −5.37 μA, and −5.11 μA, respectively. Compared with bare SPE, GO-modified SPEs have greater amperage response, exhibiting higher electrochemical responsiveness. In the presence of 100 μM FZD, a cathodic peak appeared at −0.47 V, which was assigned due to the irreversible direct electrochemical reduction in the nitro groups -R-NO_2 with hydroxylamine -R-NHOH.[48] The obtained CV result was consistent with some previous reports for the electrochemical reduction of FZD.[46–49] Fig. 6b shows LSV curves recorded on bare SPE, GO-1/SPE, GO-2/SPE, and GO-3/SPE for 50 μM CAP in 0.1 M PBS (pH 5) containing 50 μM FZD at scan rate 50 mV.s^{-1}. The Red_{NO2} reduction peak current responses for bare SPE, GO-1/SPE, GO-2/SPE, and GO-3/SPE were about −9.4 μA, −20.3 μA, −24.9 μA, and −17.6 μA, respectively. All the modified SPEs possess a higher peak current response than bare SPE. Among them, the GO-2/SPE showed the highest peak current response, which could be attributed to their electronic structure offering a more favorable route for electron transfer. In addition, a difference in the reduction peak potential value of the modified SPEs was also observed. These obtained results suggest that the oxygen content and disorder degree of GO samples have decisive effects on the electrochemical catalytic activity of FZD. Therefore, all the modified electrodes will be further investigated to gain an insight into the impact of oxygen functional groups and defect density of GO on the kinetic parameters of FZD electrochemical reduction process.

The amount of GO, scan rates, the accumulation time, and the pH value of the electrolyte solution remarkably influenced the FZD electrochemical behaviors. The various amounts of modifiers were investigated by monitoring the current of reduction of FZD. Fig. S3† shows the effect of the volume of GO on the peak current in the 100 μM FZD. The results showed that the peak current reached a maximum of 6 μL and began to decline with the continued increase. This may be due to the excessive amount of GO on the electrode surface, which led to the slow electron transfer rate. Thus, the optimum volume of the GO was selected to be about 6 μL.

The effect of pH on FZD electrochemical reduction was explored for GO-1-modified SPE in the presence of 100 μM FZD over the pH range of 3.0–11.0. As shown in Fig. S4,† LSV curves of furazolidone (100 μM) in PBS with pH change were recorded. The pH value of electrolyte solution had significant effects on peak current and peak potential. Moreover, as the pH value increased, the peak potential moved towards the negative potential. This indicated the participation of protons in the electrochemical reaction at GO/SPE. The reduction peak current

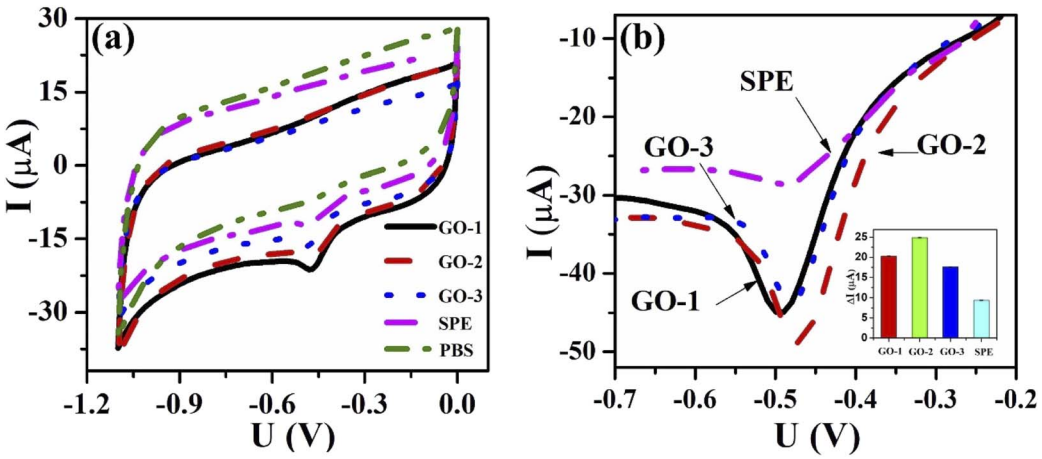

Fig. 6 (a) CV curves recorded on SPE in 0.1 M PBS (pH 7) within the absence and presence 100 μM FZD; (b) LSV curves of bare SPE, GO-1/SPE, GO-2/SPE, and GO-3/SPE in 0.1 M PBS (pH 5) containing 50 μM FZD at scan rate 50 mV s^{-1}; Insert bar chart diagram of reduction peak current responses for FZD over different modified SPEs.

increased with pH until reaching the maximum value of 27.5 μA for the pH value of 5. Then, the reduction current gradually decreased. This signifies that the H^+ ions played a key role in the electrocatalytic reduction of FZD.[46] The influence of the accumulation time on the peak current in the 100 μM furazolidone solution was exhibited in Fig. S5.† GO/SPE was investigated from 30 to 150 s to determine the optimum accumulation time. The peak current gradually increased with time and reached a maximum value at 120 s. After 120 s there was no significant change in the peak current owing to the adsorption capacity of furazolidone on the electrode surface-reaching saturation state. Consequently, the optimal accumulate time and pH were set at 120 s and pH = 5 for further experiments, respectively.

To further study the dynamic nature of the redox reactions on the electrode surface, the influence of scan rate on the electrochemical behaviors of FZD at the modified electrode surface was also investigated by CV measurements in 0.1 M PBS containing 100 μM of FZD. As shown in Fig. 7(a–c), one could observe that the cathodic peak current increased with increasing scan rate in the scanning range from 10 to 60 mV.s^{-1}. Meanwhile, the cathodic peak current (I_{pc}) showed a good linear relationship with scan rate (Fig. 7d–f). These results illustrated that the electrochemical reduction of FZD at the GO/SPE was regulated by the adsorption-controlled process. The FZD adsorption capacity on the modified electrode surface was determined through the following equation: $i_p = n^2F^2Av\Gamma/4RT$. Where F is the Faraday's constant, R is the gas constant, T is the temperature (K), A is EASA, v is the potential scan rate. From the obtained slope values, the FZD adsorption capacity (Γ) values were calculated to be 0.945 × 10^{-6} mol cm^{-2} for GO-1/SPE, 0.89 × 10^{-6} mol cm^{-2} for GO-2/SPE, and 0.87 × 10^{-6} mol cm^{-2} for GO-3/SPE. Clearly, GO-1 sample with higher oxygen functional groups content showed a higher FZD adsorption capacity, while GO-3 sample had the lowest FZD adsorption capacity. The oxygen functional groups on GO surface could form strong hydrogen-bonding interaction with NO_2 groups in FZD, which could improve the adsorption capacity towards FZD.[14] Notably, the cathodic peak potential was shifted towards the negative direction in a linear relationship with ln(v), as shown in Fig. 8. For the adsorption-controlled irreversible electrode process, the kinetic parameters (α, k_s) could be calculated based on Laviron's equation:[50–52]

$$E_{pc} = E^0 + (RT/\alpha nF) \times \ln(k_sRT/\alpha nF) - (RT/\alpha nF)\ln(v)$$

where, E^0 is the formal potential, which is represented by the intercept of the plots of E_{pc} *versus* v, as shown in Fig. S6.† From the plots of E_{pc} *versus* ln v, the linear regression equations were obtained to be $E_{pc} = -0.0165 \ln v - 0.532$ ($R^2 = 0.99$) for GO-1, $E_{pc} = -0.03 \ln v - 0.556$ ($R^2 = 0.99$) for GO-1, $E_{pc} = -0.023\ln v - 0.54$ ($R^2 = 0.99$) for GO-3. According to the slope and intercept of these regression equations, the values of electron transfer rate constant (k_s) were calculated to be about 0.37 for GO-1/SPE, 0.59 for GO-2/SPE, and 0.43 for GO-3/SPE. The values of the transfer coefficient (α) were determined through the following equation: $\Delta E_{pc,1/2} = 0.0625/n\alpha$. Where n is the number of electrons participated, $\Delta E_{pc,1/2}$ is changed in haft-peak potential ($\Delta E_{pc,1/2} = E_{pc} - E_{pc,1/2}$). The values of the transfer coefficient (α) were about 0.26 for GO-1/SPE, 0.3 for GO-2/SPE, and 0.27 for GO-3/SPE. In a comparison of kinetic parameters, the GO-2 sample showed the highest electron transfer rate constant and transfer coefficient than other modified SPEs. The k_s values

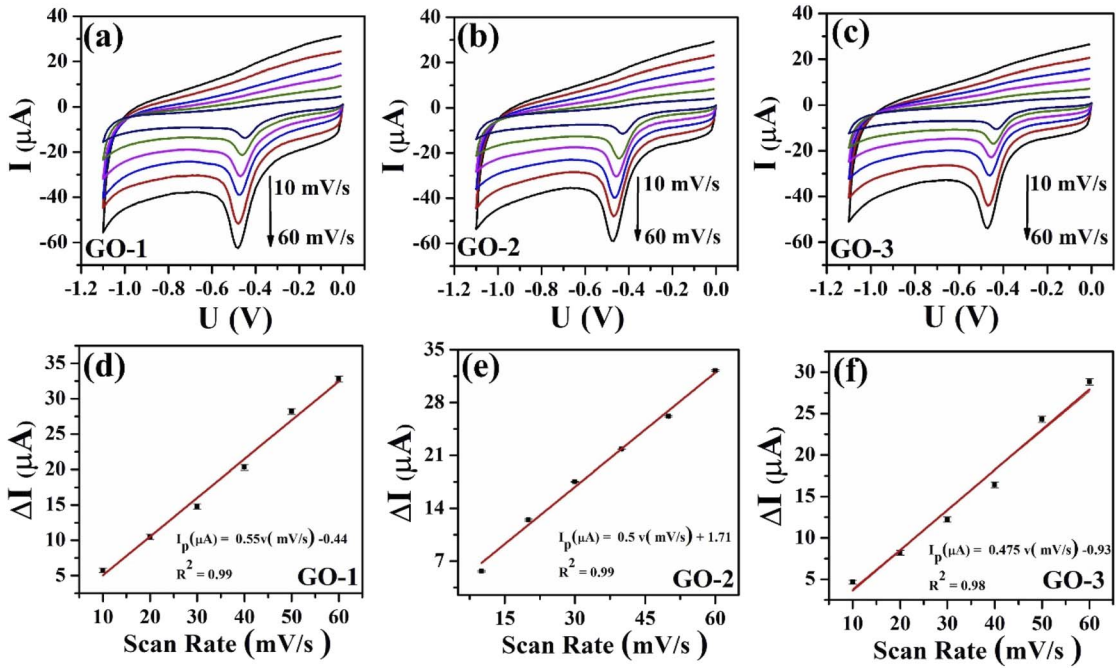

Fig. 7 (a–c) CV curves recorded of 100 μM FZD in 0.1 M PBS (pH 5.0) with various scan rates from 10 to 60 mV s^{-1}; and (d–f) the calibration plots of cathodic current response *vs.* scan rate with error bar of GO-1/SPE, GO-2/SPE, and GO-3/SPE.

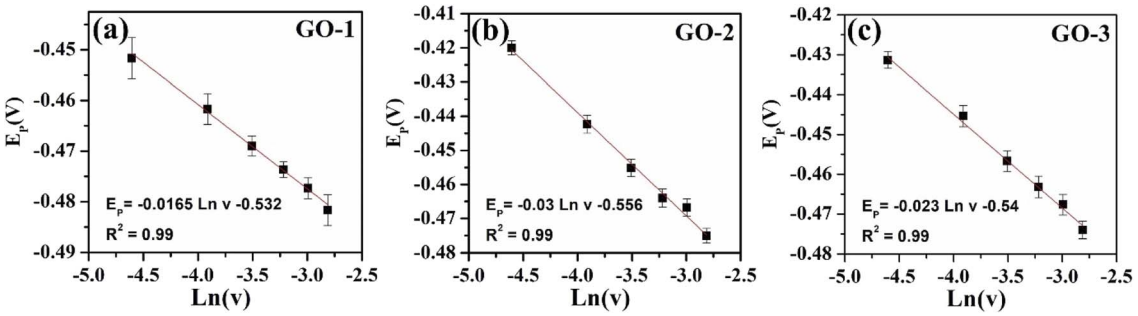

Fig. 8 The calibration plots of cathodic peak potential *vs.* natural logarithm of scan rate (ln *v*) with error bar of GO-1/SPE (a), GO-2/SPE (b), and GO-3/SPE (c).

are an estimation of the kinetic facility of the redox process, where a system with high k_s value will achieve equilibrium in a shorter period, compared to a system with low k_s value, which in this case will achieve equilibrium in a longer period.[53] The differences in the k_s, α, and Γ values could be considered as the critical factors, suggesting the obvious impact of electronic structure and oxygen functional groups content of GO on the electron transferability and effective adsorption ability between the analyte and the modified SPEs surface.

The performances of the modified SPEs for the detection of FZD were evaluated by linear sweep voltammetry (LSV). The GO-modified SPEs (GO-1/SPE, GO-2/SPE, and GO-3/SPE) were surveyed by LSV measurements in 0.1 M PBS (pH 5) with different concentrations of FZD to compare their electrochemical performances. Fig. 9 shows the LSV curves of the different FZD concentrations on the modified SPEs in 0.1 M PBS (pH 5) and the calibration plots of peak current intensity against various concentrations of FZD, respectively. It was found that the cathodic peak current increased with increasing FZD concentration for all modified SPEs. For the GO-1/SPE, the calibration curve shows a linear range from 1 to 100 μM with correlation coefficients (R^2) of 0.98. Notably, both GO-2/SPE and GO-3/SPE showed two linear segments of 1–10 μM and 10–100 μM with two different slope values. This is likely to be the consequence of the adsorption effect because the oxygen functional groups content of GO-2 and GO-3 samples were decreased.

From this linear calibration plot, the analytical parameters, including electrochemical sensitivity and limits of detection (LOD) were determined to evaluate the electrocatalytic reduction behaviors towards FZD. The LOD values of GO-1/SPE, GO-2/SPE, and GO-3/SPE were calculated to be 0.68 μM, 0.19 μM, and 0.32 μM, respectively, using the standard formula: LOD = 3SD/*S* (where SD is the standard deviation, *S* is slope value).[54] Besides

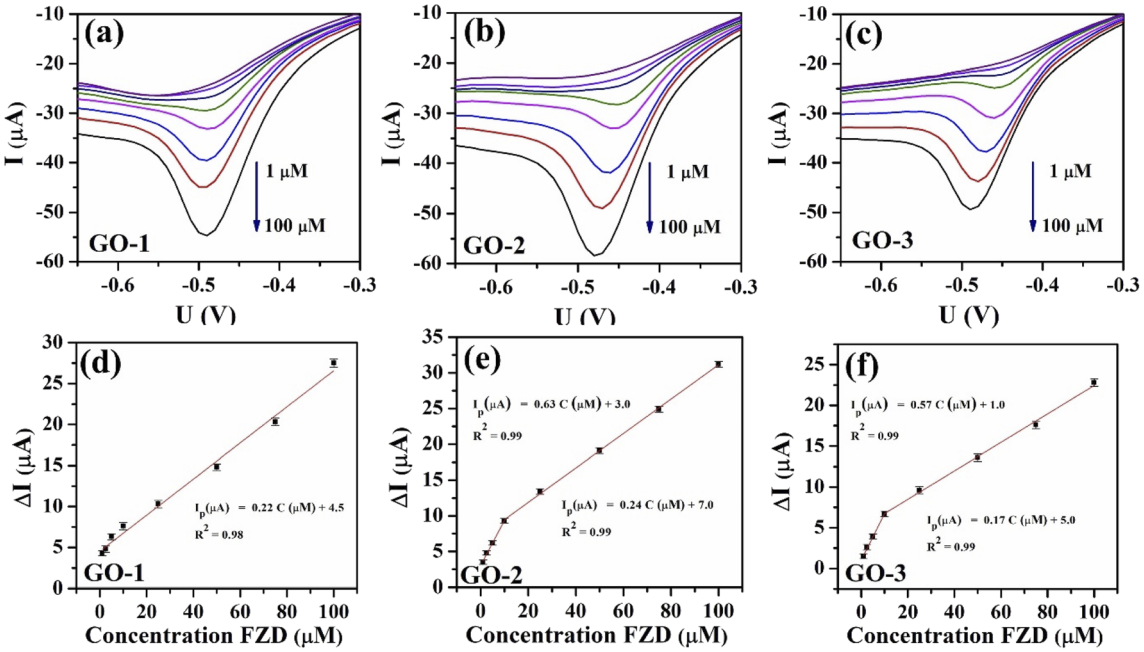

Fig. 9 (a–c) LSV curves of various concentrations of FZD in 0.1 M PBS (pH 5) at scan rate 50 mV s^{-1}; and (d–f) corresponding to the calibration plots of peak current intensity *vs.* various concentrations of FZD with error bars of GO-1/SPE, GO-2/SPE, and GO-3/SPE.

that, the electrochemical sensitivity for GO-1, GO-2, and GO-3 samples was calculated to be 0.34, 1.03, and 0.98 μA μM^{-1} cm^{-2} in the linear range of 1–100 μM, respectively. It is clear that the GO-2/SPE achieved higher electrochemical sensitivity and lower LOD in comparison with other modified SPEs. The results demonstrate that the electrocatalytic ability of GO arising from active sites on carbon framework played a main role in deciding the electrochemical reduction behaviors of FZD, especially active sites related to disordered graphitic lattice provided by the existence of sp^3 bonds.

The oxidation-reduction pathway of the FZD in the presence of GO was proposed by two processes: (1) firstly, reduction process is the formation of a nitroso intermediate (R–N═O) group from a nitro group (R–NO_2) of FZD. (2) Secondly, the next process is the rapid creation of hydroxylamine (R–NHOH).[46,55] The electrochemical mechanism of FZD was displayed as Fig. 10.

The selectivity of GO-1/SPE was examined in 50 μM of FZD containing the possible interfering compounds and ions at 4-fold concentrations. The DPV technique was carried out to investigate the influence of several cations and anions (such as, Cu^{2+}, Fe^{3+}, Ni^{2+}, SO_4^{2-}, and NO_3^-) and organic compounds (chloramphenicol (CAP), glucose, and 4-nitrophenol (4-NP)). The tested results were shown in Fig. S7.† It can be seen that some ions and various compounds did not cause significantly interference in the determination of FZD.

Besides, the LSV spectrum of GO-1/SPE using 0.1 M PBS (pH 5) containing 50 μM FZD, CAP, and 4-NP was shown in Fig. S8.† The results show that each analyte has a definite redox potential. Specifically, in the presence of 100 μM FZD, CAP, and 4-NP, the characteristic cathode peaks were recorded, appeared at −0.47 V, −0.62 V, and −0.44 V, respectively.

In order to evaluate the electrochemical detection performance of GO/SPEs in a real sample, we carried out the determination of FZD in the pork samples. The various concentrations of FZD (10, 25, and 50 μM) were spiked to the same pork samples, and then LSV measurement was used for analysis. The ultimate concentration of the FZD was calculated follows the regression equation of the calibration curves. The obtained results were summarized in Table S2.† The average recoveries for GO-1/SPE, GO-2/SPE, and GO-3/SPE were in the range from 89% to 97% with the relative standard deviations (RSD) within from 0.8% to 1.9% ($n = 3$). These results demonstrated that the electrode modified GO have good practical applicability for determination of FZD in the pork samples.

The repeatability of the modified SPEs was evaluated by recording the current response in the presence of 100 μM FZD for 10 successive times on the same electrode and condition. The relative standard deviation (RSD) of GO-1/SPE, GO-2/SPE, and GO-3/SPE were 1.07%, 1.34%, and 1.36%, respectively, as described in Fig. S9 (a–c),† which proved good repeatability of proposed electrochemical sensors.

Many previous studies indicate that improving the conductivity, electron-transfer performance, and enhancing the analyte adsorption ability of GO has been considered as practical solutions to improve detection performance for electrochemical sensors, as presented in Table 1. It has been reported that the nanopores on a basal plane of graphene have been beneficial to increasing the active area and mass transport rates.[56,57] The increase of defect density and the number of edges of graphene could accelerate the electron transfer process.[58] The removal of oxygen functional groups on the GO surface generated more active sites or rather new defects. According to Junhua Li *et al.*,[14] the strong adsorption capacity caused by the oxygen functional groups of GO with analyte could significantly improve the electrochemical response. However, the impact of oxygen functional groups content and defect density on the electrochemical behaviors did not systematically study. In this study, the GO-2 sample treated by ultrasonic irradiation showed the highest electrochemical response towards FZD owing to the high electron transfer rate and good electron transfer efficiency. This result could be attributed to the increase of active sites and number of edges under the ultrasonic irradiation, while the oxygen functional groups content did not significantly decrease.

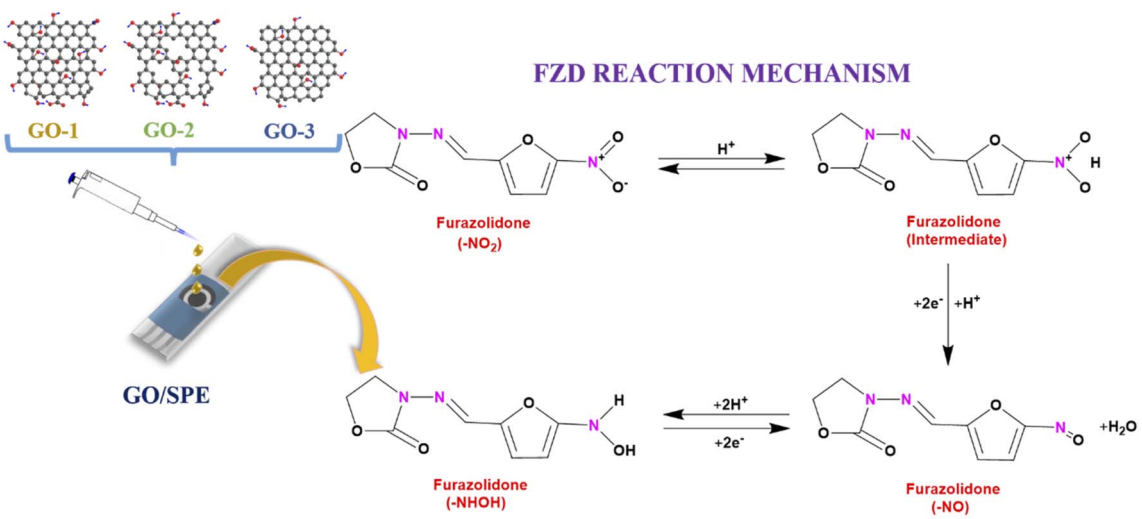

Fig. 10 Schematic illustration of the mechanism of electrochemical sensing performance of FZD using the GO-modified SPE.

Table 1 Some different synthetic methods of GO nanomaterials for the detection of different analytes in electrochemical sensing applications

Modified electrode	Synthesis method	Analyte	Technique	Enhanced mechanism	Ref.
GO/GCE	Modified hummers	4-Nitrophenol	LSV	Due to the strong adsorption capacity and large active surface area of GO	14
GO/GCE	Modified hummers	Naproxen	DPV	Effect of doping and oxygen content of different graphene oxide (GO)-based nanomaterials on their respective electrochemical behaviors	16
rGO/Fe_3O_4/GCE	Modified hummers & temperature	Nitrofurantoin (NFT)	DPV	The increased surface area, more active sites, and higher conductivity owing to the structure of rGO/Fe_3O_4NR nanocomposites	60
rGO/GCE	Hummers + ultrasonic	Ascorbic acid (AA)	DPV	rGO can enhance electron transfer activity because of its great electric conductivity and the ultrahigh surface area	61
rGO/SDS/CPE	Hummers + ultrasonic	Ambroxol	SWW	The enhancement of ambroxol adsorption on electrode surface due to rGO/SDS	62
GO/SPE	Electrochemical + ultrasonic	FZD	LSV	Defect density, the number of edges, and the oxygen-containing functional groups on the graphene oxide surface are the main factor for enhancing the electrochemical response of FZD	This work

This is similar to the research by Junyong Sun *et al.*, the electrochemical process of hollow Mn_2O_3 ellipsoids wrapped with GO was significantly enhanced for OPP and BP detection, due to the increase of active sites and surface-chemisorbed oxygen species of GO nanosheets.[59] The Raman analysis of GO-2 sample indicated the high defect levels from disordered graphitic lattice due to the existence of sp^3 bonds. The removal of oxygen functional groups and the decrease of the number of active sites on the GO by microwave irradiation caused the obvious decrease of FZD electrochemical response. Overall, the oxygen functional groups content on GO could affect the adsorption ability and electron transfer to analyte molecules, while the defect density directly impacted the rate and efficiency of electron transfer process. Therefore, instead of focusing on enhancing the adsorption capacity and large surface area, the tuning of electronic structures of GO with better electron transfer rate, more electrocatalytic sites for the reduction reactions of FZD was expected to bring higher FZD electrochemical performance.

4. Conclusions

For the first time, the roles of oxygen functional group and defect density on the analytical kinetic parameters of the FZD electrochemical reduction process was systematically studied. The ultrasound irradiation caused the fragmentation of carbon framework leading to an increase of active sites and number of edges of GO, while the microwave irradiation mainly related to removing oxygen functional groups on the GO surface. The GO-2 samples treated by ultrasound irradiation displayed higher disorder degree and defect density, compared with the untreated-GO and GO-3 samples. The GO-2/SPE sensor showed excellent electrochemical response for the detection of furazolidone in a wide linear range and the low electrochemical sensitivity (1.03 $\mu A\ \mu M^{-1}\ cm^{-2}$). Our obtained results contribute to providing further insights into the design of high-performance electrochemical sensors based on GO, thus opening up a promising new approach for monitoring FZD residues in food-producing animals.

Author contributions

D. T. N. Nga: validation, methodology, investigation, writing-original draft; N. L. N. Trang: validation, methodology, investigation, writing-original draft; H. V. Tuan: investigation, formal analysis, writing-original draft; N. X. Dinh: conceptualization, validation, investigation, writing-review & editing; P. T. Nhung: formal analysis, writing-review & editing; D. Q. Tri: investigation, validation; N. D. Cuong: investigation, validation; P. A. Tuan: methodology, validation; T. Q. Huy: methodology, validation; L. A. Tuan: conceptualization, methodology, supervision, project administration, writing-review & editing.

Conflicts of interest

The authors declare that they have no known competing financial interests or personal relationships that could have appeared to influence the work reported in this paper.

Acknowledgements

This research was supported by the Vietnam National Foundation for Science and Technology Development (NAFOSTED) through a fundamental research project (103.02–2019.01). The authors would like to acknowledge the supports with Electrochemical, Raman, UV-vis measurements from NEB Lab at the Phenikaa University; with SEM measurements from ITIMS.

References

1 R. Ramachandran, et al., A review of the advanced developments of electrochemical sensors for the detection of toxic and bioactive molecules, *Inorg. Chem. Front.*, 2019, **6**(12), 3418–3439, DOI: 10.1039/C9QI00602H.

2 N. Jadon, R. Jain, S. Sharma and K. Singh, Recent trends in electrochemical sensors for multianalyte detection – A review, *Talanta*, 2016, **161**, 894–916, DOI: 10.1016/j.talanta.2016.08.084.

3 K. Beaver, A. Dantanarayana and S. D. Minteer, Materials Approaches for Improving Electrochemical Sensor Performance, *J. Phys. Chem. B*, 2021, **125**(43), 11820–11834, DOI: 10.1021/acs.jpcb.1c07063.

4 Y. Li, J. Du, J. Yang, D. Liu and X. Lu, Electrocatalytic detection of dopamine in the presence of ascorbic acid and uric acid using single-walled carbon nanotubes modified electrode, *Colloids Surf., B*, 2012, **97**, 32–36, DOI: 10.1016/j.colsurfb.2012.03.029.

5 P. L. dos Santos, et al., Enhanced performance of 3D printed graphene electrodes after electrochemical pre-treatment: Role of exposed graphene sheets, *Sens. Actuators, B*, 2019, **281**, 837–848, DOI: 10.1016/j.snb.2018.11.013.

6 S. K. Arumugasamy, S. Govindaraju and K. Yun, Electrochemical sensor for detecting dopamine using graphene quantum dots incorporated with multiwall carbon nanotubes, *Appl. Surf. Sci.*, 2020, **508**, 145294, DOI: 10.1016/j.apsusc.2020.145294.

7 S. Su, S. Chen and C. Fan, Recent advances in two-dimensional nanomaterials-based electrochemical sensors for environmental analysis, *Green Energy Environ.*, 2018, **3**(2), 97–106, DOI: 10.1016/j.gee.2017.08.005.

8 S. Aftab, M. F. Khan, P. Gautam, H. Noh and J. Eom, MoTe2 van der Waals homojunction p–n diode with low resistance metal contacts, *Nanoscale*, 2019, **11**(19), 9518–9525, DOI: 10.1039/c8nr10526j.

9 S. Aftab, et al., Lateral PIN (p-MoTe2/Intrinsic-MoTe2/n-MoTe2) Homojunction Photodiodes, *ACS Appl. Nano Mater.*, 2022, **5**(5), 6455–6462, DOI: 10.1021/acsanm.2c00559.

10 T. N. Pham, et al., Insight into the Influence of Analyte Molecular Structure Targeted on MoS 2 -GO-Coated Electrochemical Nanosensors, *Langmuir*, 2021, **37**(41), 12059–12070, DOI: 10.1021/acs.langmuir.1c01853.

11 T. Gan, et al., Morphology–dependent electrochemical activity of Cu2O polyhedrons and construction of sensor for simultaneous determination of phenolic compounds with graphene oxide as reinforcement, *Sens. Actuators, B*, 2019, **282**, 549–558, DOI: 10.1016/j.snb.2018.11.102.

12 T. Gan, J. Li, H. Li, Y. Liu and Z. Xu, Synthesis of Au nanorod-embedded and graphene oxide-wrapped microporous ZIF-8 with high electrocatalytic activity for the sensing of pesticides, *Nanoscale*, 2019, **11**(16), 7839–7849, DOI: 10.1039/c9nr01101c.

13 L. Zhang, et al., A high-performance voltammetric methodology for the ultra-sensitive detection of riboflavin in food matrices based on graphene oxide-covered hollow MnO_2 spheres, *Food Chem.*, 2021, **352**, 129368, DOI: 10.1016/j.foodchem.2021.129368.

14 J. Li, D. Kuang, Y. Feng, F. Zhang, Z. Xu and M. Liu, A graphene oxide-based electrochemical sensor for sensitive determination of 4-nitrophenol, *J. Hazard. Mater.*, 2012, **201–202**, 250–259, DOI: 10.1016/j.jhazmat.2011.11.076.

15 M. Brycht, et al., Synthesis and characterization of the thermally reduced graphene oxide in argon atmosphere, and its application to construct graphene paste electrode as a naptalam electrochemical sensor, *Anal. Chim. Acta*, 2018, **1035**, 22–31, DOI: 10.1016/j.aca.2018.06.057.

16 L. Qian, A. R. Thiruppathi, R. Elmahdy, J. van der Zalm and A. Chen, Graphene-oxide-based electrochemical sensors for the sensitive detection of pharmaceutical drug naproxen, *Sensors*, 2020, **20**(5), 1–13, DOI: 10.3390/s20051252.

17 C. Wu, D. Sun, Q. Li and K. Wu, Electrochemical sensor for toxic ractopamine and clenbuterol based on the enhancement effect of graphene oxide, *Sens. Actuators, B*, 2012, **168**, 178–184, DOI: 10.1016/j.snb.2012.03.084.

18 Y. Zhang, H. Hao and L. Wang, Effect of morphology and defect density on electron transfer of electrochemically reduced graphene oxide, *Appl. Surf. Sci.*, 2016, **390**, 385–392, DOI: 10.1016/j.apsusc.2016.08.127.

19 J. Liu, et al., A green approach to the synthesis of high-quality graphene oxide flakes *via* electrochemical exfoliation of pencil core, *RSC Adv.*, 2013, **3**(29), 11745, DOI: 10.1039/c3ra41366g.

20 B. Qi, L. He, X. Bo, H. Yang and L. Guo, Electrochemical preparation of free-standing few-layer graphene through oxidation–reduction cycling, *Chem. Eng. J.*, 2011, **171**(1), 340–344, DOI: 10.1016/j.cej.2011.03.078.

21 L. Li, D. Zhang, J. Deng, J. Fang and Y. Gou, Review—Preparation and Application of Graphene-Based Hybrid Materials through Electrochemical Exfoliation, *J. Electrochem. Soc.*, 2020, **167**(8), 086511, DOI: 10.1149/1945-7111/ab933b.

22 R. Singh, *Recent Progress in the Electrochemical Exfoliation of Colloidal Graphene: A Review*, 2021.

23 K. Krishnamoorthy, G.-S. Kim and S. J. Kim, Graphene nanosheets: Ultrasound assisted synthesis and characterization, *Ultrason. Sonochem.*, 2013, **20**(2), 644–649, DOI: 10.1016/j.ultsonch.2012.09.007.

24 Y. Zhu, S. Murali, M. D. Stoller, A. Velamakanni, R. D. Piner and R. S. Ruoff, Microwave assisted exfoliation and reduction of graphite oxide for ultracapacitors, *Carbon*, 2010, **48**(7), 2118–2122, DOI: 10.1016/j.carbon.2010.02.001.

25 A. V. Tyurnina, et al., Ultrasonic exfoliation of graphene in water: A key parameter study, *Carbon*, 2020, **168**, 737–747, DOI: 10.1016/j.carbon.2020.06.029.

26 X. Xie, Y. Zhou and K. Huang, Advances in microwave-assisted production of reduced graphene oxide, *Front. Chem.*, 2019, **7**, 355.

27 M. Vass, K. Hruska and M. Franek, Nitrofuran antibiotics: a review on the application, prohibition and residual analysis, *Veterinary medicine*, 2008, **53**(9), 469–500, DOI: 10.17221/1979-VETMED.

28 A. J. J. Amalraj and S.-F. Wang, Synthesis of transition metal titanium oxide (MTiOx, M= Mn, Fe, Cu) and its application in furazolidone electrochemical sensor, *J. Ind. Eng. Chem.*, 2022, **111**, 356–368.

29 J. Points, D. Thorburn Burns and M. J. Walker, Forensic issues in the analysis of trace nitrofuran veterinary residues in food of animal origin, *Food Control*, 2015, **50**, 92–103, DOI: 10.1016/j.foodcont.2014.08.037.

30 P. Rebelo, J. G. Pacheco, I. V. Voroshylova, A. Melo, M. N. D. S. Cordeiro and C. Delerue-Matos, Rational development of molecular imprinted carbon paste electrode for Furazolidone detection: theoretical and experimental approach, *Sens. Actuators, B*, 2021, **329**, 129112, DOI: 10.1016/j.snb.2020.129112.

31 U. K. Sur, et al., Synthesis and characterization of stable aqueous dispersions of graphene, *Bull. Mater. Sci.*, 2016, **39**(1), 159–165, DOI: 10.1007/s12034-015-0893-0.

32 Y. Yang, et al., Controllable reduction of graphene oxide by electron-beam irradiation, *RSC Adv.*, 2019, **9**(7), 3597–3604, DOI: 10.1039/C8RA06797J.

33 R. J. Nemanich, G. Lucovsky and S. A. Solin, Infrared active optical vibrations of graphite, *Solid State Commun.*, 1977, **23**(2), 117–120, DOI: 10.1016/0038-1098(77)90663-9.

34 K. N. Kudin, B. Ozbas, H. C. Schniepp, R. K. Prud'homme, I. A. Aksay and R. Car, Raman spectra of graphite oxide and functionalized graphene sheets, *Nano Lett.*, 2008, **8**(1), 36–41, DOI: 10.1021/nl071822y.

35 B. Ma, R. D. Rodriguez, A. Ruban, S. Pavlov and E. Sheremet, The correlation between electrical conductivity and second-order Raman modes of laser-reduced graphene oxide, *Phys. Chem. Chem. Phys.*, 2019, **21**(19), 10125–10134, DOI: 10.1039/c9cp00093c.

36 L. A. Pérez, N. Bajales and G. I. Lacconi, Raman spectroscopy coupled with AFM scan head: A versatile combination for tailoring graphene oxide/reduced graphene oxide hybrid materials, *Appl. Surf. Sci.*, 2019, **495**, 143539, DOI: 10.1016/j.apsusc.2019.143539.

37 S. Claramunt, A. Varea, D. López-Díaz, M. M. Velázquez, A. Cornet and A. Cirera, The importance of interbands on the interpretation of the raman spectrum of graphene oxide, *J. Phys. Chem. C*, 2015, **119**(18), 10123–10129, DOI: 10.1021/acs.jpcc.5b01590.

38 D. López-Díaz, M. López Holgado, J. L. García-Fierro and M. M. Velázquez, Evolution of the Raman Spectrum with the Chemical Composition of Graphene Oxide, *J. Phys. Chem. C*, 2017, **121**(37), 20489–20497, DOI: 10.1021/acs.jpcc.7b06236.

39 N. Kumar and V. C. Srivastava, Simple Synthesis of Large Graphene Oxide Sheets *via* Electrochemical Method Coupled with Oxidation Process, *ACS Omega*, 2018, **3**(8), 10233–10242, DOI: 10.1021/acsomega.8b01283.

40 N. Kumar, S. Das, C. B. Sudesh and G. D. Varma, Effect of graphene oxide doping on superconducting properties of bulk MgB2, *Supercond. Sci. Technol.*, 2013, **26**(9), DOI: 10.1088/0953-2048/26/9/095008.

41 N. X. Dinh, et al., Ultrasensitive determination of chloramphenicol in pork and chicken meat samples using a portable electrochemical sensor: Effects of 2D nanomaterials on the sensing performance and stability, *New J. Chem.*, 2021, **45**(17), 7622–7636, DOI: 10.1039/d1nj00582k.

42 S. W. Chook, et al., Antibacterial performance of Ag nanoparticles and AgGO nanocomposites prepared via rapid microwave-assisted synthesis method, *Nanoscale Res. Lett.*, 2012, **7**(–7), 1, DOI: 10.1186/1556-276X-7-541.

43 B. D. Ossonon and D. Bélanger, Synthesis and characterization of sulfophenyl-functionalized reduced graphene oxide sheets, *RSC Adv.*, 2017, **7**(44), 27224–27234, DOI: 10.1039/c6ra28311j.

44 J. B. Raoof, F. Chekin, R. Ojani, S. Barari, M. Anbia and S. Mandegarzad, Synthesis and characterization of ordered mesoporous carbon as electrocatalyst for simultaneous determination of epinephrine and acetaminophen, *J. Solid State Electrochem.*, 2012, **16**(12), 3753–3760, DOI: 10.1007/s10008-012-1807-3.

45 W.-C. Wu, H.-W. Chang and Y.-C. Tsai, Electrocatalytic detection of dopamine in the presence of ascorbic acid and uric acid at silicon carbide coated electrodes, *Chem. Commun.*, 2011, **47**(22), 6458, DOI: 10.1039/c1cc11162k.

46 T. Kokulnathan, T. J. Wang, E. A. Kumar, V. Suvina and R. G. Balakrishna, Development of an Electrochemical Platform Based on Nanoplate-like Zirconium Phosphate for the Detection of Furazolidone, *ACS Appl. Nano Mater.*, 2020, **3**(5), 4522–4529, DOI: 10.1021/acsanm.0c00594.

47 Y. Sun, G. I. N. Waterhouse, L. Xu, X. Qiao and Z. Xu, Three-dimensional electrochemical sensor with covalent organic framework decorated carbon nanotubes signal amplification for the detection of furazolidone, *Sens. Actuators, B*, 2020, **321**, 128501, DOI: 10.1016/j.snb.2020.128501.

48 K.-Y. Hwa, T. S. K. Sharma and P. Karuppaiah, Development of an electrochemical sensor based on a functionalized carbon black/tungsten carbide hybrid composite for the detection of furazolidone, *New J. Chem.*, 2019, **43**(30), 12078–12086, DOI: 10.1039/C9NJ02531F.

49 A. J. Jesu Amalraj, N. M. Umesh and S. F. Wang, Synthesis of core-shell-like structure SnS_2-SnO_2 integrated with graphene nanosheets for the electrochemical detection of furazolidone drug in furoxone tablet, *J. Mol. Liq.*, 2020, **313**, 113554, DOI: 10.1016/j.molliq.2020.113554.

50 E. Laviron, General expression of the linear potential sweep voltammogram in the case of diffusionless electrochemical systems, *J. Electroanal. Chem. Interfacial Electrochem.*, 1979, **101**(1), 19–28, DOI: 10.1016/S0022-0728(79)80075-3.

51 N. T. Anh, et al., ZnO/ZnFe 2 O 4 nanocomposite-based electrochemical nanosensors for the detection of furazolidone in pork and shrimp samples: exploring the role of crystallinity, phase ratio, and heterojunction formation, *New J. Chem.*, 2022, **46**(15), 7090–7102, DOI: 10.1039/d1nj05837a.

52 U. Solaem Akond, K. Barman, A. Mahanta and S. Jasimuddin, Electrochemical Sensor for Detection of p-Nitrophenol Based on Nickel Oxide Nanoparticles/α-Cyclodextrin Functionalized Reduced Graphene Oxide,

Electroanalysis, 2021, **33**(4), 900–908, DOI: **10.1002/elan.202060450**.

53 M. M. Foroughi, S. Jahani and M. Rajaei, Facile Fabrication of 3D Dandelion-Like Cobalt Oxide Nanoflowers and Its Functionalization in the First Electrochemical Sensing of Oxymorphone: Evaluation of Kinetic Parameters at the Surface Electrode, *J. Electrochem. Soc.*, 2019, **166**(14), B1300–B1311, DOI: **10.1149/2.0511914jes**.

54 M. Yadav, V. Ganesan, R. Gupta, D. K. Yadav and P. K. Sonkar, Cobalt oxide nanocrystals anchored on graphene sheets for electrochemical determination of chloramphenicol, *Microchem. J.*, 2019, **146**, 881–887, DOI: **10.1016/j.microc.2019.02.025**.

55 T. Kokulnathan, et al., Construction of Lanthanum Vanadate/Functionalized Boron Nitride Nanocomposite: The Electrochemical Sensor for Monitoring of Furazolidone, *ACS Sustainable Chem. Eng.*, 2021, **9**(7), 2784–2794, DOI: **10.1021/acssuschemeng.0c08340**.

56 Z. Chen, Y. Zhang, J. Zhang and J. Zhou, Electrochemical Sensing Platform Based on Three-Dimensional Holey Graphene for Highly Selective and Ultra-Sensitive Detection of Ascorbic Acid, Uric Acid, and Nitrite, *J. Electrochem. Soc.*, 2019, **166**(10), B787–B792, DOI: **10.1149/2.1111910jes**.

57 Z. Chen, Y. Zhang, Y. Yang, X. Shi, L. Zhang and G. Jia, Hierarchical nitrogen-doped holey graphene as sensitive electrochemical sensor for methyl parathion detection, *Sens. Actuators, B*, 2021, **336**, 129721, DOI: **10.1016/j.snb.2021.129721**.

58 Y. Yang, Z. Chen, Q. Wang, Q. Wang and Y. Zhang, Electrochemical Sensors Based on Reduced Holey Graphene for Detection of Carbendazim, *Phys. Status Solidi*, 2022, **219**(1), 2100412, DOI: **10.1002/pssa.202100412**.

59 J. Sun, L. Xu, Z. Shi, Q. Zhao, H. Wang and T. Gan, Morphology-tunable hollow Mn2O3 nanostructures: highly efficient electrocatalysts and their electrochemical sensing for phenolic endocrine disruptors *via* toughening of graphene oxide, *Sens. Actuators, B*, 2021, **327**, 128889, DOI: **10.1016/j.snb.2020.128889**.

60 B. He and J. Li, A sensitive electrochemical sensor based on reduced graphene oxide/Fe3O4 nanorod composites for detection of nitrofurantoin and its metabolite, *Anal. Methods*, 2019, **11**(11), 1427–1435, DOI: **10.1039/c9ay00197b**.

61 H. Wang, et al., Simultaneous determination of dopamine, uric acid and ascorbic acid using a glassy carbon electrode modified with reduced graphene oxide, *RSC Adv.*, 2014, **4**(51), 26895–26901, DOI: **10.1039/c4ra03148b**.

62 S. D. Bukkitgar, N. P. Shetti, K. R. Reddy, T. A. Saleh and T. M. Aminabhavi, Ultrasonication and electrochemically-assisted synthesis of reduced graphene oxide nanosheets for electrochemical sensor applications, *FlatChem*, 2020, **23**, DOI: **10.1016/j.flatc.2020.100183**.